Crystallization kinetics in a glass-forming hybrid metal halide perovskite

Akash Singh,[1,2] *David B. Mitzi*[*,1,3]

[1]Department of Mechanical Engineering and Materials Science, Duke University, Durham, North Carolina 27708, United States

[2]University program in Materials Science and Engineering, Duke University, Durham, North Carolina 27708, United States

[3]Department of Chemistry, Duke University, Durham, North Carolina 27708, United States

[*]Corresponding author: david.mitzi@duke.edu

Final Published Manuscript: A. Singh, D. B. Mitzi, *ACS Materials Letters* 2022, *4*, 1840-1847; https://doi.org/10.1021/acsmaterialslett.2c00495

ABSTRACT: The recent discovery of glass forming hybrid metal halide perovskite (MHP) semiconductors has opened the opportunity to explore their utility beyond the already celebrated fields of photovoltaics and light emitters, as enabled by their crystalline counterparts. Reversible switching phenomenon between glassy and crystalline states further extends the potential application space to prospectively memory, computing, photonics, metamaterials and phase change energy storage. To better identify the characteristic switching properties, the underlying kinetics of glass crystallization is studied for an exemplary glass forming (S)-(−)-1-(1-naphthyl)ethylammonium lead bromide (SNPB) perovskite using a combination of calorimetry, microscopy, and kinetic modelling techniques. The study shows an activation energy of ~350 kJ/mol for the glass-crystalline transition and an Avrami parameter $n = 2.02 \pm 0.11$, pointing to heterogenous surface mediated nucleation of crystallites with 2-dimensional laminar growth in space. These results serve as an initial guide towards modelling the glass-crystallization kinetic effects in MHPs and to facilitate assessing the suitability of the glass forming MHPs for a broad range of prospective applications.

Glasses represent an important class of metastable solids, finding versatile utility in modern civilization.[1 2 3] Various compositions within different families of glass forming materials, such as oxides,[4] chalcogenides,[5] metals,[6] organic,[7] and polymeric[8] systems, have broad-ranging exploitable properties for applications ranging from packaging systems,[9] batteries,[10] solar cells,[11] catalysts,[12] photo[13]/nuclear[14] detectors, and communication devices.[15] Good glass formers such as silicate glasses don't generally crystallize under practical timescales upon providing thermal energy.[16] However, certain materials with stronger ordering tendency, e.g. some chalcogenide glasses, readily undergo reversible glass-crystal switching with thermal, optical, or electrical cycling.[17] Crystal-glass switching opens up a broader range of applications for such materials due to the distinct properties in the glass and crystalline states—e.g., memory,[17, 18] computing,[19] metamaterials[20] and photonic devices.[20-22] Though chalcogenides are the most broadly studied family of switchable glass forming semiconductors, recent demonstration of glass formation in a hybrid organic-inorganic metal halide perovskite (MHP)[23, 24] unlocks new areas of scientific enquiry and prospective application for these materials beyond the already well-celebrated fields of photovoltaics,[25] detectors[26] and emitters[27] engendered by their crystalline counterparts. Related demonstration of glass formation in metal organic frameworks (MOFs)[28] and non-halide based hybrid perovskites[29] has also spurred the field to push the boundaries of associated hybrid glasses.

Thermodynamics and kinetics underlie reversibility in glass-crystal switching. A crystalline material can liquify at temperatures beyond the melting point (T_m) (assuming congruent melting) and then be quenched to form a glass if crystallization can be circumvented during cooling. The obtained glass can then be provided with sufficient thermal energy to induce a glass transition (T_g) wherein it enters a supercooled liquid state prior to its subsequent crystallization

(T_x).[30] The above-mentioned iteration of melting (thermodynamics) and quenching/crystallization (kinetics) reflects reversibility for the process. The characteristic temperatures, i.e., T_g, T_x and T_m, serve as a guide to identify the suitability of the glass for various applications. For example, a higher T_g/T_m (Turnbull criteria of glass formation) suggests a stronger glass forming ability, with larger timescales for the ordering kinetics.[31] The associated sluggish crystallization can be employed in making optical fibers for communication,[32] glass-crystal composites,[33] or in phase change energy storage applications wherein slow release of energy may be beneficial.[34, 35] Smaller Turnbull criteria values signify higher propensity towards crystallization and associated higher crystallization rates, which may be useful in, for example, phase change memory and computing.[19] Thus, kinetic effects represent a key factor dictating the ultimate utility of an associated glass.

In this regards, understanding and controlling the kinetics of the glass-crystal transformation (i.e., nucleation and growth of crystalline grains within the hybrid glass) for the important MHP semiconductor family [36] should allow for programming of tailored properties and guide device fabrication/operation over the lifecycle of prospective switching devices—e.g., such study should aid in understanding: i) vitrification and devitrification processes in different temperature/time regimes, ii) nucleation density and crystal growth rates, iii) type of nucleation: homogeneous vs heterogeneous or sporadic vs instantaneous, iv) crystal growth mechanism and growth dimensionality, and v) feasibility of different MHP compositions targeted towards specified applications. To provide a first example of such studies for MHPs, in this article we employ iterative calorimetric measurements on the recently discovered chiral two-dimensional (2D) MHP, [S-(−)-1-(1-naphthyl)ethylammonium]$_2$PbBr$_4$ (SNPB),[23, 37] which exhibits a Turnbull criterium $T_g/T_m = 0.76$,[23] to understand the kinetics of the glass-crystal transformation. The kinetic

behavior is modelled using the Ligero[38, 39] and Kissinger[40, 41] analytical theory of glass-crystal transformation, employing calorimetric experiments to help extract the two most valuable kinetic parameters, i.e., activation energy (E) and Avrami factor (n). Extraction of these parameters elucidates the mechanism of SNPB glass crystallization. Further, the analytical results are corroborated using a set of *in-situ* and *ex-situ* microscopy to provide a firmer understanding of the nucleation and crystal growth processes.

Figure 1a shows the X-ray diffraction (XRD) pattern of SNPB crystals and the associated melt-quenched glassy counterpart. The broad hump centered at 2θ of 5.6° shows the amorphous nature of the SNPB glass as opposed to regularly repeating crystalline peaks corresponding to the (00l) family of interlayer atomic planes in SNPB crystals. The slight shift of the diffraction peak towards higher 2θ (from 4.6˚ to 5.6˚) upon glass formation suggests that some aspect of the layered nature of the crystalline phase is carried over to the glass, albeit with some structural contraction along the stacking direction.[42] The differential scanning calorimetry (DSC) and thermogravimetric (TGA) heating scans for SNPB, as provided in our previous work [23] and reproduced as Figure S1, shows the characteristic temperatures, such as glass transition temperature ($T_g \approx 67$ ˚C), crystallization onset temperature ($T_x \approx 101$ ˚C), and melting temperature ($T_m \approx 175$ ˚C), which are all significantly less than the degradation onset temperature ($T_d \approx 205$ ˚C), allowing for an appropriate working temperature range for vitrification and devitrification of the SNPB glass.

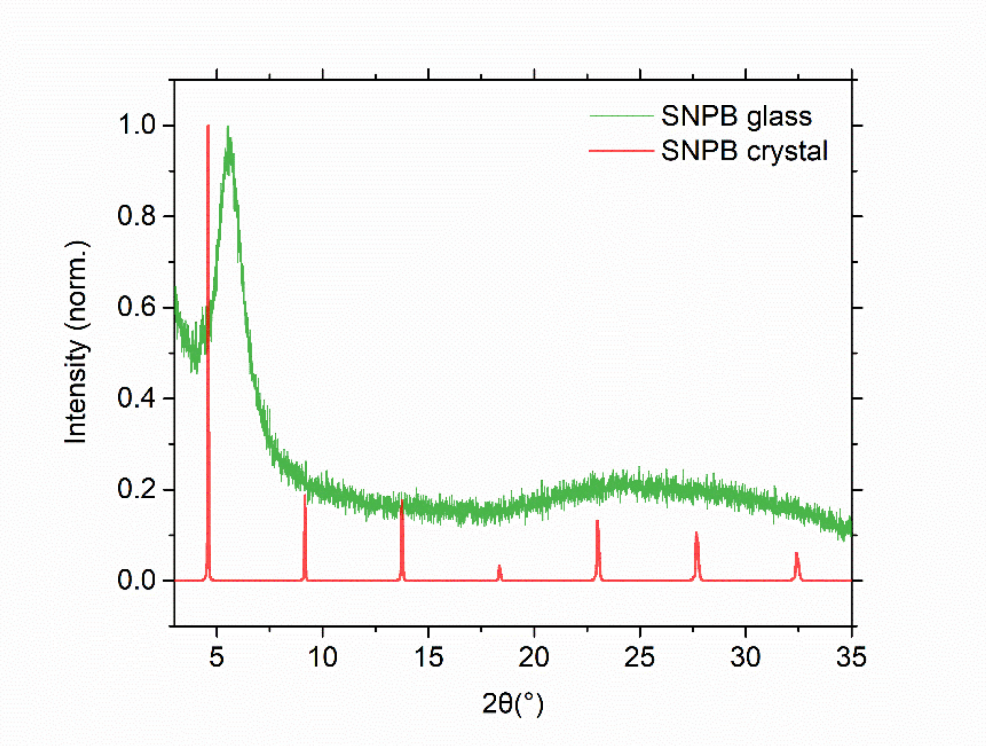

Figure 1. X-ray diffraction pattern of SNPB crystals (red curve) and SNPB glassy film (green curve). The SNPB crystals show a regularly repeating pattern of (00l) features with primary peak at 2θ of 4.6°, whereas the SNPB glass shows a typical amorphous broad feature centering at 2θ of 5.6°. The other broad feature (20-35°) in the green curve arises predominantly from the underlying soda-lime glass substrate.

Upon confirming the complete glass formation (XRD) and the associated regimes of working temperatures (DSC and TGA), multiple crystallization data modelling theories were examined to select the optimum range for extraction of associated parameters.[30, 43] The available models each have pros and cons depending upon the glass-forming system under study and the conditions employed for the study. The fundamental theory dates to the 1930s, was independently developed by Johnson, Mehl and Avrami, and is known as the JMA kinetics model.[44-46] Under *isothermal* conditions, the JMA theory of crystallization kinetics can be expressed as,

$$x(t) = 1 - exp[-(Kt)^n] \qquad (i)$$

where x represents the crystallized volume fraction at a certain time (t) corresponding to a given isotherm; n is the Avrami coefficient, which can be split into a summation of n_d (dimensionality of the crystal growth) and n_n (nucleation mechanism); and K is a reaction constant that can further be expressed by equation (ii).

$$K = K_0\, e^{(-E/RT)} \qquad (ii)$$

where R is the gas constant, T is the absolute temperature, E is the activation energy for the overall crystallization process, which includes both the nucleation and growth, and K_o is known as the frequency factor, which is related to the likelihood of a molecular entity participating in the process of crystallization and overcoming the energy barrier E. Importantly, K has temperature dependence, but under isothermal conditions this parameter can be considered a constant. When equation (i) is written in its logarithmic form, it can be expressed as,

$$\ln(-\ln(1 - x)) = \ln(K) + n\ln(t) \qquad (iii)$$

which on plotting may yield a straight line with slope represented by the Avrami coefficient, n.[46] The crystallized volume fraction (x) as a function of time (t) can be accessed by converting the DSC crystallization exotherm peak into various discrete area segments, each covering some interval of time.[30]

Equations (*i*)-(*iii*) show how the JMA theory applies to isothermal crystallization. However, there are practical limitations in experimentally obtaining a suitable exothermic crystallization curve during an isothermal hold step in a calorimetric experiment (e.g., see Figure S2 for the case of data collected for the current SNPB hybrid material), thus suggesting the need for non-isothermal methods. Non-isothermal methods have added advantages, as they are i) time efficient (no need to equilibrate at each temperature), ii) not subject to potential temperature over/under-shoot and oscillation during the process of rapid ramp to the isothermal temperature and, iii) able to measure phase transformations that occur too rapidly to be measured under isothermal conditions.[30, 47] The JMA theory can be extended to *non-isothermal* conditions only in cases where the nucleation centers can be shown to form before or during the initial stages of crystal growth and where the crystal growth rate can be considered Arrhenian in the determined temperature range of crystallization.[30, 48, 49] The former condition is supported for the SNPB glass through *in-situ* microscopy (described later), whereas Arrhenian growth can be assumed for measurement in the relatively narrow temperature window[49] (i.e., ~373-393 K) over which the activation energy remains nominally constant during the glass-crystal transformation process.[30] Both conditions for use of the non-isothermal approach appear to be satisfied, as shown by the experimental results discussed below.

Hence, the non-isothermal mode of calorimetric experiments can be employed for the current study of SNPB glass crystallization. Such JMA theory extensions were provided by Ligero[38, 39] and Kissinger.[40, 41] The Ligero method provides the kinetic parameters—e.g., Avrami coefficient (*n*) and the activation energy (*E*)—at different crystallized volume fractions of glass

(x) and under non-isothermal conditions,[38] by taking the logarithm of the first order derivative of both sides of equations (*i*) and (*ii*) with respect to time (t), as defined in equation (*iv*).

$$\ln\left(\frac{dx}{dt}\right) = \ln[K_O f(x)] - \frac{E}{RT} \qquad (iv)$$

Here, f(x) is a function of the Avrami coefficient (n) and the crystallized volume fraction (x), as described in equation (*v*).

$$f(x) = n(1-x)\,[-\ln(1-x)]^{\frac{n-1}{n}} \qquad (v)$$

As evident from equation (*iv*), for constant values of ln[K_0f(x)], the activation energy (E) can be determined from the slope of the ln(dx/dt) vs inverse temperature ($1/T$) plot. Further, using equations (*iv*) and (*v*), when we can consider ln[K_0f(x)] = C (constant), then for two crystallized fractions x_1 and x_2 that satisfy this condition, the value of Avrami coefficient can be determined using the expression described by,[38, 39]

$$n = \ln\left[\frac{\ln(1-x_2)}{\ln(1-x_1)}\right].\left[\ln\left[\frac{(1-x_2)\ln(1-x_2)}{(1-x_1)\ln(1-x_1)}\right]^{-1}\right] \qquad (vi)$$

The other widely employed approach, the Kissinger model, which is a non-isothermal extension of Arrhenius and reaction rate equations,[41] considers the change in peak crystallization temperature (T_p) as a function of heating rate (q_h). The simplicity of the model facilitates the extraction of activation energy (E) using equation (*vii*).[30, 40]

$$\ln\left(\frac{q_h}{T_p^2}\right) = \ln\left(\frac{ZR}{E}\right) - \frac{E}{RT_p} \qquad (vii)$$

where, R is the gas constant and Z is a pre-exponential factor from the Arrhenius equation. The Kissinger model provides the activation energy corresponding to the crystallization fraction with highest crystallization rate, i.e., peak of the crystallization exotherm. The extracted value is often found to closely match with the value extracted from the Ligero analysis.[39, 50]

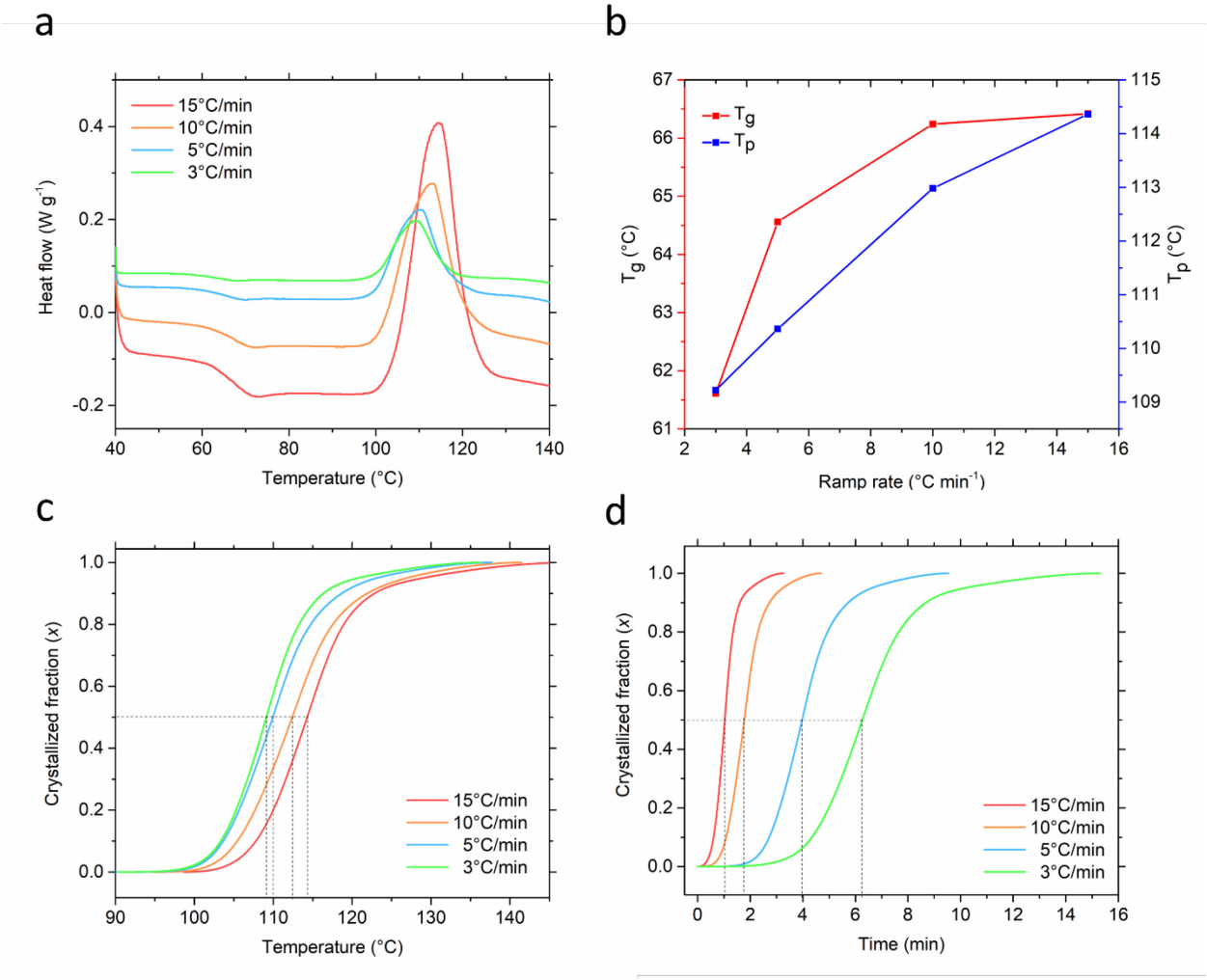

Figure 2. Differential Scanning Calorimetry (DSC) measurements and analysis of SNPB glass. a) The crystallization exotherms obtained at ramp rates of 3, 5, 10 and 15°C/min. b) The change in the glass transition temperature (T_g) and crystallization peak temperature (T_p) as a function of

heating ramp rates. The evolution of crystallized volume fraction as a function of temperature (c) and time (d). The dotted lines show the temperatures and times corresponding to 50 % crystallized volume (x = 0.5).

The DSC crystallization exotherms of SNPB monolithic glass are obtained at ramp rates of 3, 5, 10 and 15 °C/min (Figure 2a) in a hermetically sealed aluminum pan. Crystallization at these ramp rates yields comparable enthalpy values (Table S1). Figure 2b shows the change in glass transition temperature (T_g) and crystallization exotherm peak temperature (T_p) values on employing different ramp rates, which reveals the underlying kinetic effects involved in the glass-crystal transformation. The crystallization exothermic peaks (Figure 2a) are integrated at different temperature and time intervals to obtain the crystallized volume fraction (x) as a function of temperature (Figure 2c) and time (Figure 2d), showing the typical sigmoidal shape of crystallization.[43]

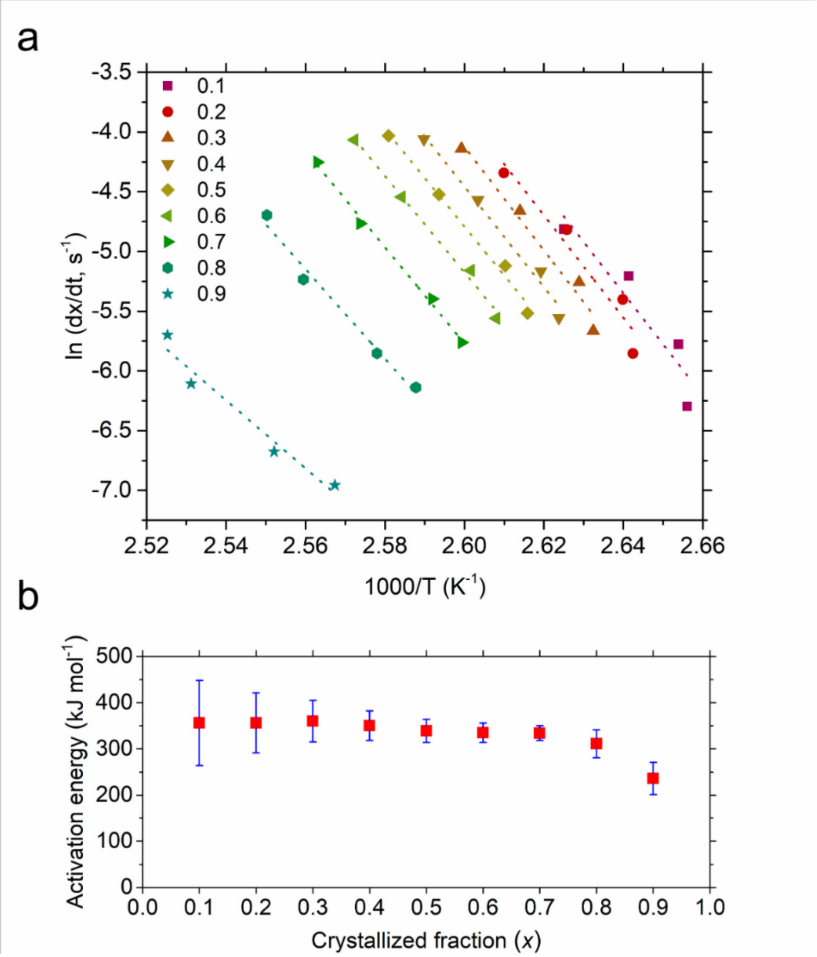

Figure 3. The Ligero kinetic analysis. a) Ligero curves corresponding to different crystallized volume fractions (0.1-0.9) along with their linear fits. The four points in each linear fit correspond to different ramp rates, with the bottom and top ones measured at 3 and 15°C/min, respectively. b) Extracted activation energy with standard deviation at various stages of crystallization.

The crystallized volume fraction curves obtained in Figure 2d are then processed using the Ligero method employing equation (*iv*) (Figure 3a) and plotted for crystallized volume fraction ranging from 0.1 to 0.9, and the corresponding activation energy of crystallization is obtained through the slope of the curve. The derived activation energy (i.e., from the slope of curves in Figure 3a) is depicted in Figure 3b with square root mean error (R^2) shown in Table S2. The

activation energy in the most well-behaved linear regime (for $x = 0.7$, for which the R^2 is greater than 0.99) is determined to be 334 kJ/mol with standard deviation of 21 kJ/mol. Furthermore, upon performing the Kissinger analysis (using equation (*vii*)), the extracted activation energy of 365 $\pm$ 25 kJ/mol (Figure S3) is in good agreement with the Ligero analysis. Activation energies of crystallization as well as the glass forming ability may vary significantly within a glass forming family, depending on detailed composition and element choice.[51, 52] Nevertheless, just for perspective, the above activation energies can be compared with analogous values for some oxide glasses (strong glass formers) that may range from ~300 to 700 kJ/mol [53-56] and chalcogenide glasses such as germanium-antimony-telluride (GST) used in phase change applications (poor glass formers) that may range from ~150-300 kJ/mol.[57-59] This value could further be lowered at higher temperatures due to the breakdown of Arrhenian behavior.[57, 60] Hence, a direct comparison of activation energies between different families of glass formers may not be meaningful. Nevertheless, the extraction of activation energies does serve as a starting point to understand the differences in the kinetics of glass formation among different prospective compositions in the family of glass forming MHPs. Further, the extracted fragility index $m \sim 45$ (Figure S4, calculated from the change in T_g in Figure 2) suggests a strong glass forming behaviour.[42]

Having gained confidence in the extracted activation energies by using both Ligero and Kissinger models, we next consider the extended Ligero approach to determine the Avrami parameter (n), which may reflect the nucleation mechanism and crystal growth dimensionality. For this analysis, two values of crystallized volume fractions (x_1 and x_2) are required wherein, between these two fractions, the value of $\ln[K_0 f(x)]$ should be a constant, considering the linear nature of equation (*iv*). The plot relating $\ln[K_0 f(x)]$ and crystallized fraction (x) for different ramp rates show such a

behavior, with a near constant value of $\ln[K_0 f(x)]$ for a broader range of x (Figure S5). As can be seen from Figure 3b, for $x = 0.7$, the slope of equation (*iv*) yields the highest degree of linear fit with $R^2 = 0.9955$ (Table S2). Upon determining the $\ln[K_0 f(x)]$ value corresponding to this fraction, taken as $x_2 = 0.7$, the value of x_1 is identified corresponding to the same value of $\ln[K_0 f(x)]$ for each ramp rate (Figure S5). The values of the Avrami factor (n), calculated using equation (*vi*), are tabulated (Table S3) and averaged to yield a value of 2.02 ± 0.11. The Avrami factor being close to 2 suggests that the SNPB glass nucleates either with constant nucleation rate and 1-dimensional growth or with fixed number of nucleating sites (site saturation) and 2-dimensional growth.[30] The growth mechanism can be hypothesized as being interface controlled (and not diffusion controlled) due to the similar composition of glass/melt and the crystals (congruently melting system with single recrystallized phase, *such as ours*), which allows for predominantly interfacial local change in atomic arrangement.[61] The integral value (~2) of Avrami factor further validates this hypothesis.[30, 49] The various possible nucleation and growth mechanisms correspond to different Avrami factors (n), as detailed in Table S4 for reference. Accounting for the 2D nature of the final crystalline material, the value of $n = 2$ from DSC analysis suggests a marginally low degree of overlap between the nucleation and growth processes[60] and a 2D growth mechanism for the crystalline grains.

To bolster the above claim regarding nucleation and growth, we present electron microscopic images of SNPB melt-quenched films with different degrees of crystallization. Figure 4a-d shows top-view SEM images of the glassy films crystallized at 120°C for different duration of times (complete crystallization is achieved in 5 min). The cross-sectional images show a uniform morphology for the glassy films. Crystallization appears to nucleate heterogeneously at

the surface and the fully crystalline films show a 2D morphology through the plate-like growth (Figure 4e-f), in accord with the Avrami parameter obtained through calorimetric data modelling. To further address the nucleation mechanism, melt quenched SNPB glassy films were prepared and examined by *in-situ* optical microscopy at an isothermal hold temperature of 120°C. The optical images as a function of time (Figure 5) and corresponding supplementary Video S1 show the emergence of a nominally fixed number of nuclei. After site saturation, these nucleation centers grow in time with no substantial emergence of newer isolated sites, confirming a fixed heterogenous nucleation mechanism as the primary nucleation pathway. A spin-coated amorphous SNPB film was also prepared and subjected to crystallization at the same temperature for 5 minutes. Figure S6 shows the optical image, revealing complete crystallization at the rough edges of the soda-lime glass substrates, whereas incomplete crystallization was observed near the smoother central region, suggesting a heterogeneous surface- or edge-dominated nucleation mechanism.

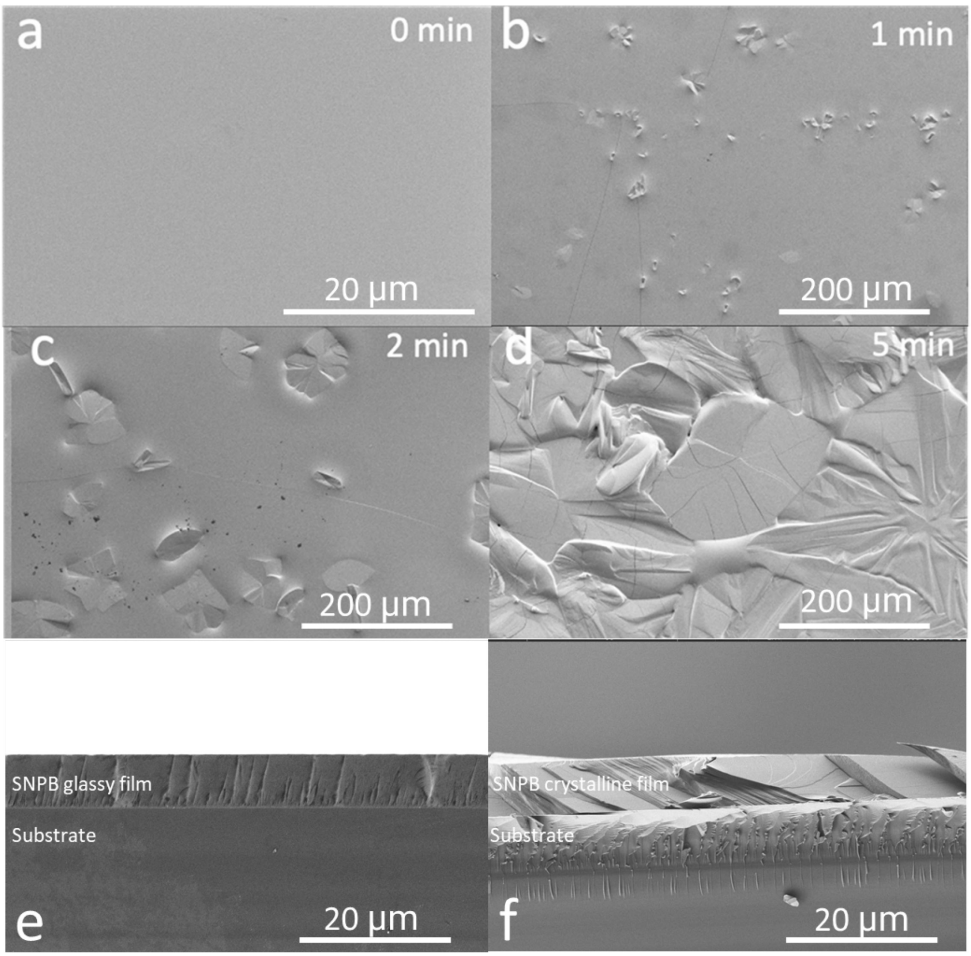

Figure 4. Scanning electron microscopy (SEM) images of partially crystallized SNPB films. a-d) Top-view SEM images of melt-quenched SNPB glassy films annealed (ex situ) at 120°C for different duration. e-f) Cross-sectional SEM images of SNPB glassy film before and after complete crystallization at 120°C for 5 minutes.

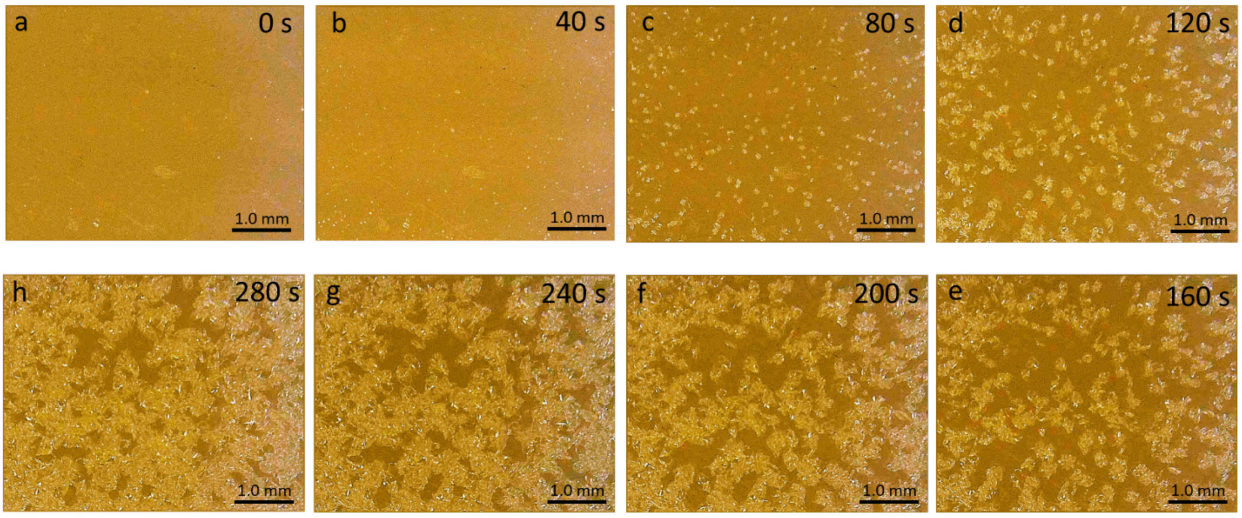

Figure 5. In-situ optical microscopy of glassy SNPB film during heating. a-h) Top-view optical microscope images of melt quenched SNPB glassy film at various stages of isothermal crystallization at 120°C. Stills are obtained from Supplementary Video S1.

As an additional pathway for elucidating the effect of surfaces/interfaces on crystallization, we performed DSC heating scans on SNPB glass samples with three different form factors or particle sizes—i.e., monolith, flakes, and powder (Figure S7 and S8). This study shows two clear trends: a) increasing propensity towards crystallization (nucleation) for smaller feature size, with T_p shifting to lower values and, b) increasing crystallization peak intensities (indicative of higher nucleation density) as the SNPB glass particle size is reduced from bulk monolith to flakes to finely powdered configuration (progressing to higher surface-to-volume ratio). These trends reveal the underlying surface-dominated nucleation mechanism[56, 62-66] and are not unique to SNPB, but have been observed in other glass forming systems.[62, 66] Importantly, there are two features in the DSC profile of flakes and powdered glass samples. We hypothesize that the narrow feature corresponds to sudden nucleation (shifts to lower temperature with reduction in particle size from

flakes to powder), whereas the broad feature corresponds to crystal growth. For monolith configuration, these two processes are convoluted, which leads to a single exothermic crystallization peak (Figure S9).[67] The morphological study provides further evidence of growth dominated (after rapid fixed nucleation) crystallization behavior in SNPB glass, akin to the observations in the AgInSbTe (AIST) chalcogenide phase change material. In AIST, crystallization proceeds with formation of a few nuclei in the nucleation stage that further grow larger during the later growth stages, whereas GST shows nucleation dominated behavior with formation of myriad number of nuclei before a short growth process.[68] Interestingly, due to the heterogeneous surface mediated nucleation in the SNPB glass, it is conceivable to control the number of nucleation sites by either modifying the surface area or through introduction of a varying density of foreign surfaces (e.g., particles) that can act as nucleating sites. The modification of introduced nucleation site density may provide an additional degree of control for the glass-crystal transformation timescale. However, the reduction in T_g and T_x to near ambient temperature for very small sized glass particles may also limit their utility (inadvertent switching due to thermal fluctuations); design of MHPs with higher T_g and T_x values can be targeted, given the rich compositional space of organic cations from which to choose.[69]

In summary, for the first time we report the underlying kinetics governing the glass-crystal transformation in an exemplary MHP, [S-(−)-1-(1-naphthyl)ethylammonium]$_2$PbBr$_4$ (SNPB). The iterative calorimetric experiments coupled with Ligero and Kissinger kinetic models enable extraction of the activation energy for crystallization (E = 334 $\pm$ 21 kJ/mol and 365 $\pm$ 25 kJ/mol respectively, for the two models) and the Avrami parameter (n = 2.02 $\pm$ 0.11), which sheds light on the nucleation and crystal growth mechanisms. The determination of the activation energy will

ultimately (as new glass forming MHPs are discovered) facilitate comparing the glass forming ability and the stability of the various systems. Moreover, optical microscope and SEM images have been used at different stages of glass crystallization to corroborate the results obtained from the DSC kinetic models, revealing that crystallization proceeds through heterogenous surface driven nucleation followed by 2D growth. These results serve as an initial guide towards understanding and modelling glass-crystallization kinetic effects in MHPs. With continued discovery of new glass forming MHP compositions, the disparate requirements for glass formation and distinct crystallization characteristics are expected to aid in the design and fabrication of prospective broad-ranging devices employing such systems.

ASSOCIATED CONTENT

Supporting Information

Methods, Differential scanning calorimetry (DSC) and thermogravimetric analysis of SNPB glass, Isothermal crystallization of SNPB glass at various temperatures, Kissinger analysis of glass-crystallization activation energy, Fragility index plot, Avrami factor (*n*) calculation plot, Optical microscope image of partially crystallized spin-coated SNPB glassy film, DSC analysis of SNPB glass with different particle sizes, Optical photographs of SNPB glass with different particle sizes, Two consecutive DSC heating scans of finely powdered SNPB glass, Table for crystallization enthalpy, Table for activation energy at different crystallized volume fraction, Table with Avrami (*n*) parameter, Table with nucleation and growth mechanism.

Supporting Video S1

Supporting Video.mp4

AUTHOR INFORMATION

***Corresponding Author**

David B. Mitzi – Email: david.mitzi@duke.edu; orcid.org/0000-0001-5189-4612;

ACKNOWLEDGEMENT

This work was supported by the National Science Foundation under Grant No. DMR- 2114117.

The work was performed in part at the Duke University Shared Materials Instrumentation Facility (SMIF), a member of the North Carolina Research Triangle Nanotechnology Network (RTNN), which is supported by the National Science Foundation (Grant ECCS-2025064) as part of the National Nanotechnology Coordinated Infrastructure.

REFERENCES

1. Macfarlane, A.; Martin, G., A world of glass. *Science* **2004,** *305*, 1407-1408.
2. Morse, D. L.; Evenson, J. W., Welcome to the glass age. *Int. J. Appl. Glass Sci.* **2016,** *7*, 409-412.
3. Zachariasen, W. H., The atomic arrangement in glass. *J. Am. Chem. Soc.* **1932,** *54*, 3841-3851.
4. Kurkjian, C. R.; Prindle, W. R., Perspectives on the history of glass composition. *J. Am. Ceram. Soc.* **1998,** *81*, 795-813.
5. Ovshinsky, S., The science of atomic engineering of chalcogenide glasses. *Phys. Status Solidi B* **2009,** *246*, 1741-1743.
6. Byrne, C. J.; Eldrup, M., Bulk metallic glasses. *Science* **2008,** *321*, 502-503.
7. Swallen, S. F.; Kearns, K. L.; Mapes, M. K.; Kim, Y. S.; McMahon, R. J.; Ediger, M. D.; Wu, T.; Yu, L.; Satija, S., Organic glasses with exceptional thermodynamic and kinetic stability. *Science* **2007,** *315*, 353-356.
8. Guo, Y.; Morozov, A.; Schneider, D.; Chung, J. W.; Zhang, C.; Waldmann, M.; Yao, N.; Fytas, G.; Arnold, C. B.; Priestley, R. D., Ultrastable nanostructured polymer glasses. *Nat. Mater.* **2012,** *11*, 337-343.
9. Schaut, R. A.; Weeks, W. P., Historical review of glasses used for parenteral packaging. *PDA J. Pharm. Sci. Technol.* **2017,** *71*, 279-296.
10. Wei, Z.; Wang, D.; Yang, X.; Wang, C.; Chen, G.; Du, F., From crystalline to amorphous: An effective avenue to engineer high-performance electrode materials for sodium-ion batteries. *Adv. Mater. Interfaces* **2018,** *5*, 1800639.

11. Carlson, D. E.; Wronski, C. R., Amorphous silicon solar cell. *Appl. Phys. Lett.* **1976,** *28*, 671-673.
12. Brower, W.; Matyjaszczyk, M.; Pettit, T.; Smith, G., Metallic glasses as novel catalysts. *Nature* **1983,** *301*, 497-499.
13. Huang, C.-Y., The effect of Gamma irradiation on the stability of amorphous InGaZnO metal-semiconductor-metal UV photodetectors. *J. Non-Cryst. Solids* **2020,** *546*, 120292.
14. Aschenbach, J.; Fiedler, G.; Schreck-Köllner, H.; Siegert, G., Special glasses as energy detectors for fission fragments. *Nucl. Instrum. Methods* **1974,** *116*, 389-395.
15. Agrawal, G. P., *Fiber-optic communication systems*. John Wiley & Sons: 2012.
16. Le Losq, C.; Cicconi, M. R.; Greaves, G. N.; Neuville, D. R., Silicate glasses. In *Springer Handbook of Glass*, Springer: 2019; pp 441-503.
17. Zhang, W.; Mazzarello, R.; Wuttig, M.; Ma, E., Designing crystallization in phase-change materials for universal memory and neuro-inspired computing. *Nature Rev. Mater.* **2019,** *4*, 150-168.
18. Wuttig, M.; Yamada, N., Phase-change materials for rewriteable data storage. *Nat. Mater.* **2007,** *6* , 824-832.
19. Ielmini, D.; Wong, H.-S. P., In-memory computing with resistive switching devices. *Nature Electron.* **2018,** *1*, 333-343.
20. Wang, Q.; Rogers, E. T.; Gholipour, B.; Wang, C.-M.; Yuan, G.; Teng, J.; Zheludev, N. I., Optically reconfigurable metasurfaces and photonic devices based on phase change materials. *Nature Photonics* **2016,** *10*, 60-65.
21. Eggleton, B. J.; Luther-Davies, B.; Richardson, K., Chalcogenide photonics. *Nat. Photonics* **2011,** *5*, 141-148.
22. Wuttig, M.; Bhaskaran, H.; Taubner, T., Phase-change materials for non-volatile photonic applications. *Nat. Photonics* **2017,** *11*, 465-476.
23. Singh, A.; Jana, M. K.; Mitzi, D. B., Reversible crystal–glass transition in a metal halide perovskite. *Adv. Mater.* **2021,** *33*, 2005868.
24. Singh, A.; Jana, M.; Mitzi, D. B., Organic-inorganic metal halide glass. US Patent App. 17/333,862: 2022.
25. Best Research-Cell Efficiency Chart, https://www.nrel.gov/pv/cell-efficiency.html (accessed: June 2022).
26. Wang, H. P.; Li, S.; Liu, X.; Shi, Z.; Fang, X.; He, J. H., Low-dimensional metal halide perovskite photodetectors. *Adv. Mater.* **2021,** *33*, 2003309.
27. Lin, K.; Xing, J.; Quan, L. N.; de Arquer, F. P. G.; Gong, X.; Lu, J.; Xie, L.; Zhao, W.; Zhang, D.; Yan, C., Perovskite light-emitting diodes with external quantum efficiency exceeding 20 per cent. *Nature* **2018,** *562*, 245-248.
28. Fonseca, J.; Gong, T.; Jiao, L.; Jiang, H.-L., Metal-organic frameworks (MOFs) beyond crystallinity: amorphous MOFs, MOF liquids and MOF glasses. *J. Mater. Chem. A* **2021,** *9*, 10562-10611.
29. Shaw, B. K.; Hughes, A. R.; Ducamp, M.; Moss, S.; Debnath, A.; Sapnik, A. F.; Thorne, M. F.; McHugh, L. N.; Pugliese, A.; Keeble, D. S.; Chater, P.; Garcia, J. M. B.; Moya, X.; Saha, S. K.; A. Keen, D.; Coudert, F.-X.; Blanc, F.; Bennett, T. D., Melting of hybrid organic–inorganic perovskites. *Nat. Chem.* **2021,** *13*, 778–785.
30. Zheng, Q.; Zhang, Y.; Montazerian, M.; Gulbiten, O.; Mauro, J. C.; Zanotto, E. D.; Yue, Y., Understanding glass through differential scanning calorimetry. *Chem. Rev.* **2019,** *119*, 7848-7939.

31. Turnbull, D., Under what conditions can a glass be formed? *Contemporary Physics* **1969,** *10*, 473-488.
32. Cozmuta, I.; Rasky, D. J., Exotic Optical Fibers and Glasses: Innovative Material Processing Opportunities in Earth's Orbit. *New Space* **2017,** *5*, 121-140.
33. Hou, J.; Ashling, C. W.; Collins, S. M.; Krajnc, A.; Zhou, C.; Longley, L.; Johnstone, D. N.; Chater, P. A.; Li, S.; Coulet, M.-V., Metal-organic framework crystal-glass composites. *Nat. Commun.* **2019,** *10*, 2580.
34. Lilley, D.; Menon, A. K.; Kaur, S.; Lubner, S.; Prasher, R. S., Phase change materials for thermal energy storage: A perspective on linking phonon physics to performance. *J. Appl. Phys.* **2021,** *130*, 220903.
35. McGillicuddy, R. D.; Thapa, S.; Wenny, M. B.; Gonzalez, M. I.; Mason, J. A., Metal–organic phase-change materials for thermal energy storage. *J. Am. Chem. Soc.* **2020,** *142*, 19170-19180.
36. Saparov, B.; Mitzi, D. B., Organic–inorganic perovskites: structural versatility for functional materials design. *Chem. Rev.* **2016,** *116*, 4558-4596.
37. Jana, M. K.; Song, R.; Liu, H.; Khanal, D. R.; Janke, S. M.; Zhao, R.; Liu, C.; Vardeny, Z. V.; Blum, V.; Mitzi, D. B., Organic-to-inorganic structural chirality transfer in a 2D hybrid perovskite and impact on Rashba-Dresselhaus spin-orbit coupling. *Nat. Commun.* **2020,** *11*, 4699.
38. Ligero, R.; Vázquez, J.; Villares, P.; Jiménez-Garay, R., A study of the crystallization kinetics of some Cu-As-Te glasses. *J. Mater. Sci.* **1991,** *26*, 211-215.
39. Rodrigues, A.; Narváez-Semanate, J.; Cabral, A.; Rodrigues, A., Determination of crystallization kinetics parameters of a $Li_{1.5}Al_{0.5}Ge_{1.5}(PO_4)_3$ (LAGP) glass by differential scanning calorimetry. *Mater. Res.* **2013,** *16*, 811-816.
40. Kissinger, H. E., Variation of peak temperature with heating rate in differential thermal analysis. *J. Res. Natl. Bur. Stand. (U. S.)* **1956,** *57*, 217-221.
41. Blaine, R. L.; Kissinger, H. E., Homer Kissinger and the Kissinger equation. *Thermochim. Acta* **2012,** *540*, 1-6.
42. Slavney, A. H.; Kim, H. K.; Tao, S.; Liu, M.; Billinge, S. J.; Mason, J. A., Liquid and Glass Phases of an Alkylguanidinium Sulfonate Hydrogen-Bonded Organic Framework. *J. Am. Chem. Soc.* **2022,** *144*, 11064-11068.
43. Vyazovkin, S.; Burnham, A. K.; Criado, J. M.; Pérez-Maqueda, L. A.; Popescu, C.; Sbirrazzuoli, N., ICTAC Kinetics Committee recommendations for performing kinetic computations on thermal analysis data. *Thermochim. Acta* **2011,** *520*, 1-19.
44. Avrami, M., Kinetics of phase change. I General theory. *J. Chem. Phys.* **1939,** *7*, 1103-1112.
45. Gutzow, I. S.; Schmelzer, J. W., Kinetics of Overall Crystallization: Kinetic Criteria for Glass-Formation. In *The Vitreous State*, Springer: 2013; pp 395-415.
46. Joraid, A., Limitation of the Johnson–Mehl–Avrami (JMA) formula for kinetic analysis of the crystallization of a chalcogenide glass. *Thermochim. Acta* **2005,** *436*, 78-82.
47. Ray, C.; Zhang, T.; Reis, S.; Brow, R., Determining kinetic parameters for isothermal crystallization of glasses. *J. Amer. Ceram. Soc.* **2007,** *90*, 769-773.
48. Svoboda, R., Crystallization of glasses–When to use the Johnson-Mehl-Avrami kinetics? *J. Eur. Ceram. Soc.* **2021,** *41*, 7862-7867.
49. Málek, J., The applicability of Johnson-Mehl-Avrami model in the thermal analysis of the crystallization kinetics of glasses. *Thermochim. Acta* **1995,** *267*, 61-73.

50. Marques, L. E.; Costa, A. M.; Crovace, M. C.; Rodrigues, A. C.; Cabral, A. A., Influence of particle size on nonisothermal crystallization in a lithium disilicate glass. *J. Am. Ceram. Soc.* **2015,** *98*, 774-780.
51. Mihai, C.; Sava, F.; Simandan, I.; Galca, A.; Burducea, I.; Becherescu, N.; Velea, A., Structural and optical properties of amorphous Si–Ge–Te thin films prepared by combinatorial sputtering. *Sci. Rep.* **2021,** *11*, 11755.
52. Popescu, M.; Velea, A.; Sava, F.; Lőrinczi, A., Chalcogenide systems at the border of the glass-formation domain: A key for understanding the memory-switching phenomena. *Phys. Status Solidi B* **2014,** *251*, 1334-1339.
53. Płońska, M.; Plewa, J., Crystallization of GeO_2–Al_2O_3–Bi_2O_3 Glass. *Crystals* **2020,** *10*, 522.
54. Guo, H., Crystallization Kinetics of Bi_2O_3-SiO_2 Binary System. In *Advances in Glass Science and Technology*, IntechOpen: 2018.
55. Mazurin, O.; Leko, V.; Komarova, L., Crystallization of silica and titanium oxide-silica corning glasses (codes 7940 and 7971). *J. Non-Cryst. Solids* **1975,** *18*, 1-9.
56. Li, W.; Mitchell, B. S., Nucleation and crystallization in calcium aluminate glasses. *J. Non-Cryst. Solids* **1999,** *255*, 199-207.
57. Chen, B.; Ten Brink, G. H.; Palasantzas, G.; Kooi, B. J., Crystallization kinetics of GeSbTe phase-change nanoparticles resolved by ultrafast calorimetry. *J. Phys. Chem. C* **2017,** *121*, 8569-8578.
58. Yamada, N.; Ohno, E.; Nishiuchi, K.; Akahira, N.; Takao, M., Rapid-phase transitions of GeTe-Sb_2Te_3 pseudobinary amorphous thin films for an optical disk memory. *J. Appl. Phys.* **1991,** *69*, 2849-2856.
59. Tominaga, J.; Shima, T.; Fons, P.; Simpson, R.; Kuwahara, M.; Kolobov, A., What is the origin of activation energy in phase-change film? *Jpn. J. Appl. Phys.* **2009,** *48*, 03A053.
60. Orava, J.; Greer, A. á.; Gholipour, B.; Hewak, D.; Smith, C., Characterization of supercooled liquid $Ge_2Sb_2Te_5$ and its crystallization by ultrafast-heating calorimetry. *Nat. Mater.* **2012,** *11*, 279-283.
61. https://ocw.mit.edu/courses/materials-science-and-engineering/3-205-thermodynamics-and-kinetics-of-materials-fall-2006/lecture-notes/lecture08_slides.pdf (accessed: May 2022).
62. Kracker, M.; Vladislavova, L.; Thieme, C.; Zscheckel, T.; Thieme, K.; Höche, T.; Rüssel, C., Surface crystallization of low thermal expansion $Ba_{0.5}Sr_{0.5}Zn_2Si_2O_7$ from an $8BaO{\cdot}8SrO{\cdot}34ZnO{\cdot}50SiO_2$ glass. *RSC Adv.* **2017,** *7*, 44834-44842.
63. Karpukhina, N.; Hill, R.; Law, R., Crystallisation in oxide glasses–a tutorial review. *Chem. Soc. Rev.* **2014,** *43*, 2174-2186.
64. Casasola, R.; Pérez, J. M.; Romero, M., Surface and volume crystallization in fluorrichterite based glasses. *J. Asian Ceram. Soc.* **2020,** *8*, 642-652.
65. Teixeira, S. R.; Romero, M.; Rincón, J. M., Crystallization of SiO_2–CaO–Na_2O glass using sugarcane bagasse ash as silica source. *J. Am. Ceram. Soc.* **2010,** *93*, 450-455.
66. Ray, C. S.; Yang, Q.; Huang, W.-h.; Day, D. E., Surface and internal crystallization in glasses as determined by differential thermal analysis. *J. Am. Ceram. Soc.* **1996,** *79*, 3155-3160.
67. Lorenzo, A.; Müller, A., Estimation of the nucleation and crystal growth contributions to the overall crystallization energy barrier. *J. Polym. Sci. B: Polym. Phys* **2008,** *46*, 1478-1487.
68. Coombs, J.; Jongenelis, A.; van Es-Spiekman, W.; Jacobs, B., Laser-induced crystallization phenomena in GeTe-based alloys. I. Characterization of nucleation and growth. *J. Appl. Phys.* **1995,** *78*, 4906-4917.

69. Zhang, F.; Lu, H.; Tong, J.; Berry, J. J.; Beard, M. C.; Zhu, K., Advances in two-dimensional organic–inorganic hybrid perovskites. *Energy Environ. Sci.* **2020,** *13*, 1154-1186.

TABLE OF CONTENT GRAPHIC: